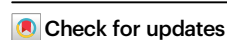












Bioresorbable, wireless dual stimulator for peripheral nerve regeneration

Received: 8 October 2024

Accepted: 29 April 2025

Published online: 22 May 2025



Hak-Young Ahn ^{1,2,28}, Jordan B. Walters ^{3,28}, Raudel Avila⁴, Seyong Oh ⁵, Seung Gi Seo^{1,2}, Jong Uk Kim^{1,2}, Jihun Park^{1,2}, Seonggwang Yoo ^{1,2,6}, Yeon Sik Choi ⁷, Tae Yeon Kim^{1,2}, Jiaqi Liu ^{1,2}, Jae-Young Yoo ⁸, Oliver Ralph Weissleder ^{1,2}, Dominic D'Andrea³, Chanh Park^{1,2}, Geumbee Lee⁹, Donghwi Cho ^{10,11}, Woo-Youl Maeng ^{1,2}, Hong-Joon Yoon ^{12,13}, Grace Wickerson^{1,2}, Yasmine Bouricha³, Jing Tian¹⁴, Tzu Chun Chung^{14,15}, Sumanas W. Jordan^{1,16,17}, Song Li ^{14,18,19,20}, Yonggang Huang ^{1,21,22,23}, Colin K. Franz ^{1,3,24,25} ✉ & John A. Rogers ^{1,2,21,22,26,27} ✉

Wireless bioresorbable electrical stimulators have broad potential as therapeutic implants. Such devices operate for a clinically relevant duration and then harmlessly dissolve, eliminating the need for surgical removal. A representative application is in treating peripheral nerve injuries through targeted stimulation at either proximal or distal sites, with operation for up to one week. This report introduces enhanced devices with additional capabilities: (1) simultaneous stimulation of both proximal and distal sites, and (2) robust operation for as long as several months, all achieved with materials that naturally resorb by hydrolysis in surrounding biofluids. Systematic investigations of the materials and design aspects highlight the key features that enable dual stimulation and with enhanced stability. Animal model studies illustrate beneficial effects in promoting peripheral nerve regeneration, as quantified by increased total muscle and muscle fiber cross-sectional area and compound muscle action potentials. These findings expand the clinical applications of bioresorbable stimulators, particularly for long-term nerve regeneration and continuous neuromodulation-based monitoring.

Peripheral nerve injuries (PNIs) can regenerate spontaneously, but the process is often slow and incomplete, leaving most patients with permanent impairments. While surgical repair and rehabilitation can promote some recovery, they are not always sufficient to achieve effective nerve regeneration. Therapeutic electrical stimulation (TES) has emerged as a promising method to enhance nerve regeneration and functional recovery, typically by applying stimulation to locations near the injury site¹. All published clinical trials on TES have used the Grass SD9 stimulator and percutaneous wire electrodes placed just proximal to the site of nerve repair^{2–5}. Although this device is widely available for research, its cumbersome design, reliance on percutaneous wires, lack of built-in stimulus isolation for safety, and absence

of precise software controls limit its clinical utility. Moreover, regulatory hurdles further restrict its widespread adoption in real-world settings, where safety, precision, and patient compliance are of paramount importance.

Recent advances in TES technology enable significant improvements in both efficacy and patient safety, with the latest examples that include wireless, programmable stimulators that enhance muscle reinnervation when used in protocols that involve daily 1-hour sessions of 20 Hz TES applied for consecutive days following nerve repair⁶. A key advantage of this implant is in the elimination of percutaneous wires, which reduces infection risks and the potential for mechanical displacement, and in its bioresorbable construction, which eliminates

A full list of affiliations appears at the end of the paper. ✉ e-mail: cfranz@srslab.org; jrogers@northwestern.edu

device load without a surgical extraction. Guo, H. et al. further refined this technology by matching the kinetics of bioresorption to clinical needs, offering short-term functionality for perioperative TES applications lasting about 1 hour, with the device degrading shortly afterward⁷.

While these TES devices have value for uses that require operation for less than 1 month^{6,8}, implants with comparatively long lifespans represent an unmet need. The bioresorbable nerve stimulators introduced here incorporate various structural and material enhancements to enable operation for up to several months, allowing for tailored TES protocols that adjust to the complexity and stage of nerve recovery. An additional unique feature is the ability to deliver stimulation at multiple nerve sites, either independently or in tandem, which is particularly beneficial in more complex injuries where multiple nerve branches may require repair. This flexibility allows for precise targeting of specific TES, tailored to the clinical scenario and with the potential to lead to more robust outcomes.

The following describes these critical features in detail. Animal model studies with the resulting optimized devices demonstrate that dual stimulation effectively promotes target muscle reinnervation, particularly by increasing muscle cross-sectional area and enhancing the reinnervation of muscle fibers. The outcomes reported here have utility not only in this context, but also in other clinical applications that require long-term treatments with bioresorbable devices.

Results

Materials and design layouts

Figure 1a illustrates the envisioned use of electrical stimulation for patients suffering from foot drop syndrome, a condition that can result from an injury to a peripheral nerve (e.g., fibular neuropathy). In this example, a bioresorbable dual stimulator interfaces with the sciatic nerve at locations adjacent to the site of the injury to accelerate recovery (Fig. 1b). Wireless operation involves magnetic inductive coupling between an external coil supplied with radio frequency power and a matched coil that is part of the implanted device. Multiple cycles of stimulation can occur at various times during the recovery process, in hospital or home settings. After this form of treatment, the device naturally resorbs in the body through hydrolysis and natural metabolic reactions, thereby eliminating the need for surgical extraction and allowing patients to return to their daily lives without an additional visit to the hospital.

The exploded-view schematic illustration in Fig. 1c highlights the structure of the device. Supplementary Figs. 1, 2 and the Methods section provide details on the materials, processing approaches and designs. The device functionally divides into (i) a receiver (R_x) coil and rectifier circuit, (ii) an extension electrode, and (iii) cuff electrodes. A unique feature, relative to previously published devices, is in the capability to stimulate sites that are both proximal and distal to the location of the injury, simultaneously through energy harvested by a single R_x coil. The magnified view shows conformal contact between these two cuff electrodes at corresponding nerve locations, as described subsequently. The interlocking folded via structure of the R_x coil (red dotted box, Fig. 2a.(i)) and the connection structure for the rectifying diode (light blue dotted box, Fig. 2a.(ii–v)) adopt optimized designs for stable operating lifetimes that significantly exceed those reported previously, as described in detail in the next section.

Figure 1d presents a photographs of the device integrated with a phantom nerve. The LEDs connect to the cuff electrodes to provide visual confirmation of the operation (top of Fig. 1d and Supplementary Fig. 3). The device can function reliably in a bent state, as illustrated on a finger (bottom of Fig. 1d). Computerized X-ray tomography images collected 2 weeks after implantation in a rat show that the device remains interfaced with the relevant anatomical structures, with no signs of damage to the device or the adjacent tissues, as in Fig. 1e.

The device slowly bioresorbs when exposed to biofluids, as illustrated in accelerated tests conducted by immersion in phosphate-buffered saline (PBS; pH 7.4) solution at 95 °C (Fig. 1f). The device mostly dissolves within 50 days, and the residual material completely disappears after 80 days. Previous studies show that the rates of bio-degradation are $\sim 4.8 \times 10^{-5}$ g/day, 1.3 $\mu\text{m}/\text{day}$, 0.02 $\mu\text{m}/\text{day}$, and 4.5 nm/day for the main constituent materials, specifically the bioresorbable dynamic covalent polyurethane (PU)⁸, polyanhydride (PA)⁹, molybdenum (Mo)¹⁰, and monocrystalline silicon (Si) nanomembranes (NMs) respectively¹¹, under physiological conditions (1 × PBS solution at pH 7.4 at 37 °C). Supplementary Fig. 1 shows details of the materials and their thicknesses. Based on expected time-temperature scaling, at physiological temperatures, complete dissolution occurs in ~ 7 months for PA, 2 years for the Mo electrode, and 2.9 years for the Si NM. For PU, considering its weight (25-mm-diameter PU 75 disks, 100 μm thick, weighing ~ 0.018 g, the time for complete degradation is 1–1.5 years. Resorption of the cuff electrode occurs first, followed by the extension electrode and the R_x coil structure, and finally, the Si diode within the R_x coil structure. In vivo, complete dissolution typically occurs more rapidly due to macrophage activity, enzymatic processes, and other biological mechanisms. These effects lead to degradation of PU within 1 year¹². Based on these considerations and previous studies, dissolution of the Mo electrodes will occur in ~ 2 years¹³. The Si NMs will dissolve within 0.5–1.5 years¹⁴. Depending on the biofluid environment, the PA will dissolve within 7 to 10 months (Supplementary Table 1)^{15,16}.

Features for long-term stable operation

Key engineering advances (Fig. 2a) reported here include optimized via structures (Fig. 2a.(i) and Supplementary Fig. 4), improved diode connection designs (Fig. 2a.(ii)–(v)), and a monolithic Mo sheet that integrates the R_x coils, extension electrodes, and cuff structures (Fig. 2a.(vi)). The results allow stable operational lifetimes that exceed those reported previously by approximately five times, when evaluated in vivo (Fig. 2e).

The first improvement involves the mechanical connection of the top and bottom R_x coils through an interlocking folded via structure (Supplementary Fig. 5a, c). This design maintains a stable quality factor (Q factor, as defined by $Q = f_r / \Delta f$, where f_r is the resonance frequency, and Δf is the full width at half-maximum (FWHM) of the resonance)^{17,18} and resonant frequency for 40 days, while the previous bonded design without mechanical connection shows a significant decrease in Q factor by day 2 and an increase in resonant frequency by approximately two times by day 40 (Fig. 2b and Supplementary Fig. 5e–g). The decrease in Q factor has a dominant effect on the output voltage (V_{out}). Consequently, the output of the device with the bonded design rapidly decreases after 5 days, whereas the folded design remains stable for 50 days.

The second improvement includes three aspects associated with the rectifying diode (Fig. 2a.(ii)–(v)): substrate material, diode pocket structure, and connection pads. First, PA replaces PU and PLGA as the substrate, to enable superior mechanical and thermal stability (Fig. 2a.(ii)). First, with a Young's modulus of ~ 25 MPa¹⁹, far exceeding that of PU (0.5–3.8 MPa)⁸, PA provides excellent integrity under mechanical stresses such as bending and stretching. Also, the higher glass transition temperature (T_g : 61 °C)²⁰ and thermal degradation temperature (T_d : ≥ 300 °C)¹⁹ of PA compared to PLGA (T_g : ~ 40 –60 °C, T_d : ~ 300 °C)¹⁰, ensure stability during bonding processes at temperatures of ~ 210 °C. resonant frequency for 40 days. Second, a recessed pocket structure secures the diode and prevents mechanical damage (Fig. 2a.(iii), Supplementary Figs. 7, 8). Third, the addition of holes and sawtooth patterns in the connection pads increases the contact areas and creates mechanical interlocking features for improved bonding with the W/wax paste (Fig. 2c and Supplementary Fig. 9e).

The third improvement involves a monolithic design, wherein a single Mo sheet forms the R_x coils, extension electrodes, and

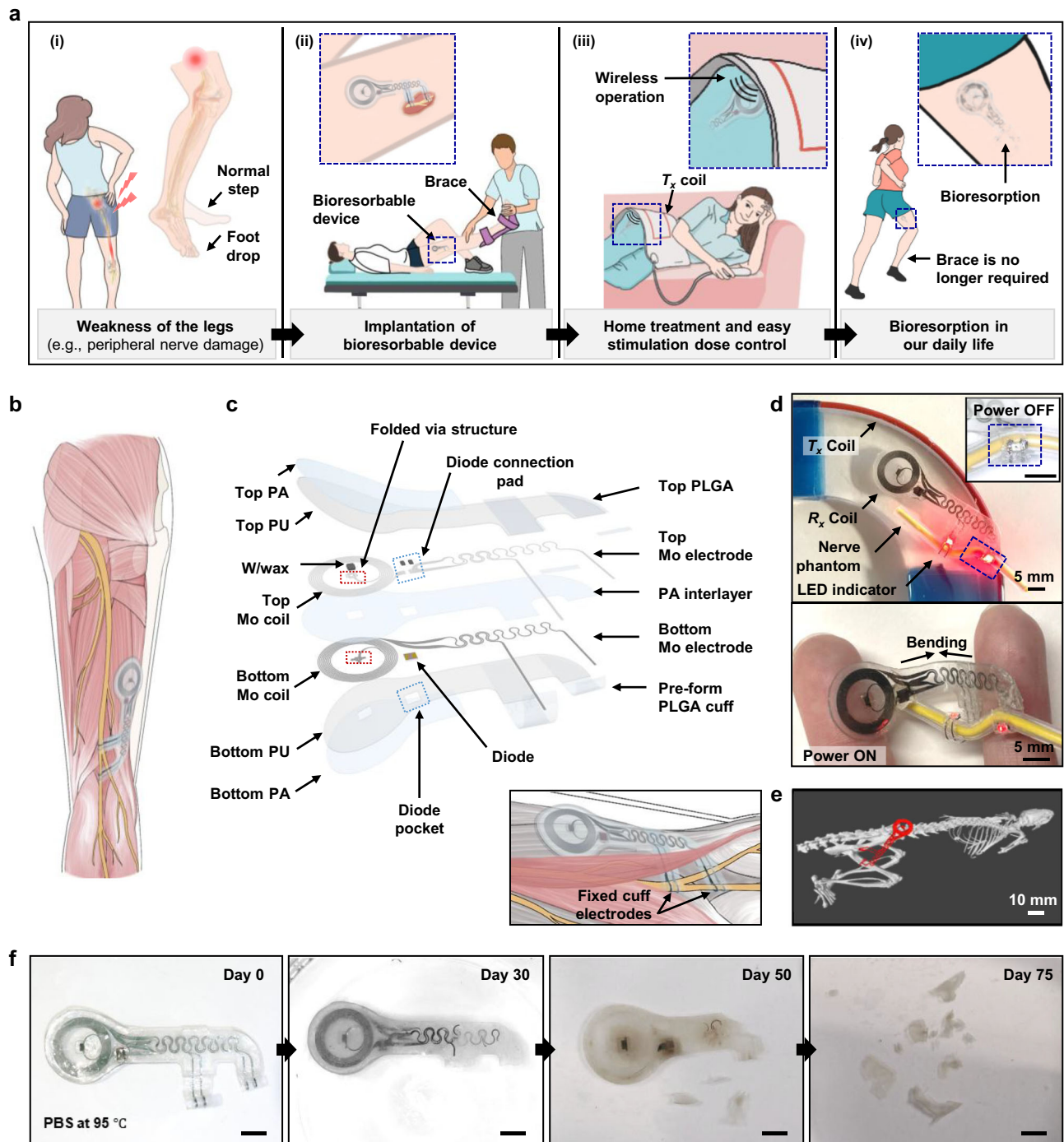


Fig. 1 | Bioresorbable wireless dual-stimulator for nerve regeneration.

a Illustrations of the overall envisioned use case for a device to accelerate recovery from a sciatic nerve injury. **b** Illustration of the site of implantation for this clinical use case. **c** Exploded-view schematic illustration of the device. **d** Photographs of the device integrated with a phantom nerve, with red indicator LEDs, resting on

part of a T_x coil (top), and in a bent state on the finger (bottom). **e** Micro-CT image of a device implanted in a rat. **f** Images of the accelerated dissolution of a device captured at various times after immersion in PBS (pH 7.4) solution at 95 °C. Scale bar, 5 mm.

cuff structures. The result is a significant enhancement in electrical and mechanical robustness compared to the bonded system (Fig. 2a.(vi) and Supplementary Fig. 10). Specifically, the connection between the R_x coil and cuff electrode withstands bending and compression during implantation (Supplementary Fig. 10c). While the bonded design fails after 28,000 cycles at 37 °C, the monolithic design exhibits negligible changes after 60,000 cycles (Fig. 2d and Supplementary Fig. 10d). Additionally, the monolithic design maintains peak strains below the yield

point during 19% uniaxial stretching, unlike the bonded device, which fails under similar conditions (Supplementary Fig. 10e, f).

Supplementary Fig. 11 highlights some additional aspects of improvements in performance. For example, the optimized design maintains uniform temperatures of 25 °C at the R_x coil and 27 °C at the diode during operation under ambient conditions, while the previous design shows uneven heating, peaking at 37 °C near the diode in a manner that affects reliability. Full performance details are in Supplementary Note 1.

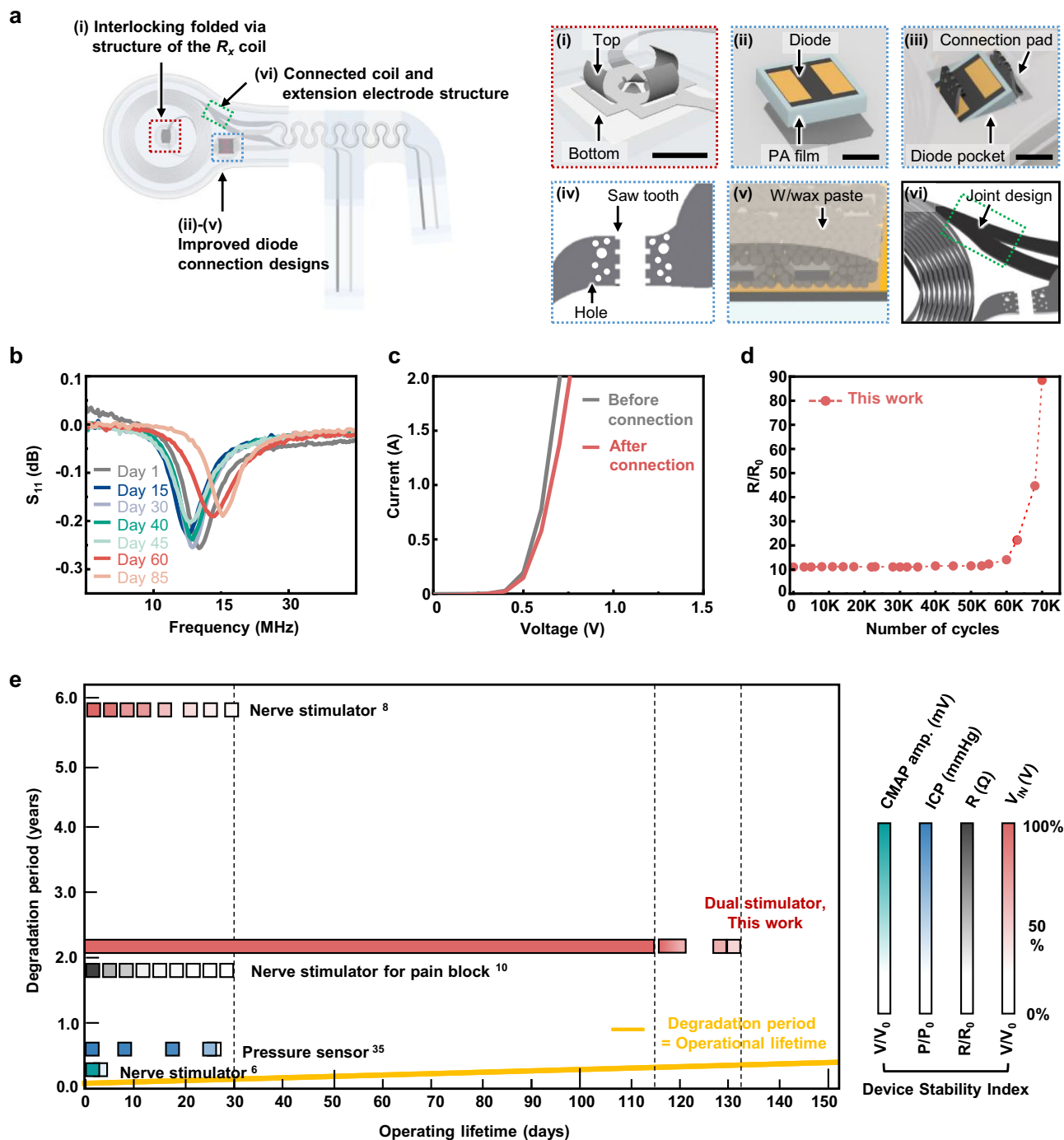


Fig. 2 | Designs for improved lifetime for stable operation. **a** Top-view schematic illustration of the device. Schematic illustrations of key engineering features, including (i) an interlocking folded via structure for joining the R_x coils, (ii) a diode transferred onto a PA substrate, (iii) a pocket for diode insertion, (iv) a diode connection pad with a hole and sawtooth structure and (v) an enlarged view of the connection with W/wax paste, (vi) a connected coil and extension electrode structure fabricated from a single sheet of Mo by a laser-cutting process. Scale bar, 1 mm. **b** Measured RF behavior (S_{11}) and resonance frequency as a function of time of immersion in $1 \times$ PBS (pH 7.4) at 37°C . **c** I-V characteristics before connection (black) and after connection (red) of the bioresorbable PIN diode. **d** Changes in resistance of serpentine traces for the optimized joined design during cyclic

loading (40% compression, 5 mm/s velocity, 70,000 cycles). **e** Comparison of the degradation period (y-axis), operating lifetime (x-axis), and the change in device stability (color change by stability index) over time for the bioresorbable devices reported here and those in previous reports. The stability index on the right displays the rate of change for each of the following parameters: (i) Maximum EMG amplitude induced by the bioresorbable stimulator over 7 days⁶, (ii) changes in intracranial pressure (ICP)³⁵, (iii) resistance changes in the electrode¹⁰, and (iv) minimum operating voltage required to induce muscle contractions⁸. The yellow solid line indicates the case where the degradation period and operational lifetime are equal.

Figure 2e presents representative studies of operating lifetime, indicating that our device maintains 100% stability for more than 1 month. The ratio of the operating lifetime (O) to the degradation period (D) increases significantly, rising from 0.6–3.2% to about 19%, as

a metric of improvement in the balance between operating lifetime and degradation period (Supplementary Tables 2, 3 and Supplementary Fig. 12). Collectively, our system offers significant advantages in functionality, stability, and performance compared to previously

reported bioresorbable nerve stimulators (Supplementary Table 4). The operating lifetimes and degradation periods of the devices can be adjusted from several weeks to several months, depending on the selection of constituent materials and layouts (details are in Supplementary Table 5).

The treatment duration for optimal recovery in clinical nerve repair is expected to exceed 6 days due to nerve size and axon regeneration distances. The device enables evoked CMAP recordings across multiple time points, allowing investigators to detect early signs of electrophysiological recovery during the process of neuromuscular reinnervation. Current FDA-approved temporary neuromuscular stimulator systems for neuropathic pain²¹ or diaphragm muscle pacing²² are designed for short-term use (≤ 60 days) and have inherent limitations, such as risk for infection due to the percutaneous leads. Also, retained internal segments of the non-resorbable leads can impact future medical care, including MRI compatibility, and limit subsequent interventions. In contrast, our implantable stimulator provides a long-lasting (> 60 days), fully resorbable solution, eliminating the need for percutaneous components, external controllers, or retrieval procedures. This is particularly advantageous for sustained neuromodulation applications, such as enhancing axon regeneration, without the drawbacks of retained foreign material or procedural complexity.

Electrical characteristics of dual stimulators

During electrical stimulation, the proximal and distal cuffs deliver the same V_{out} to both contact sites, due to their parallel connection in the overall circuit. Figure 3 shows the effects of differences in nerve resistance in an animal test setup designed to stimulate different nerve sites. Fig. 3a, b summarize the electrical characteristics, with an illustration of the locations of the two cuff electrodes, the nerve injury, and the coil for a rat model. Studies include operation of the device in proximal only (PROX), distal only (DIST), and dual (DUAL) stimulation mode, determined by the connection of the extension electrode to the cuff electrode (Fig. 3b, top row). The dual-stimulation device can selectively isolate and stimulate either the proximal or distal segments of the nerve for therapeutic electrical stimulation treatments. The dotted arrow indicates stimulation (frequency 20 Hz, applied voltage 3–5 V) of the sciatic nerve. Measurements of compound muscle action potential (CMAP) indicate a depolarizing effect only in the tibialis anterior muscle (TA) with PROX stimulation, only in the lateral gastrocnemius (LG) with DIST stimulation and in both the TA and LG with DUAL stimulation (Fig. 3b, bottom row), as expected. The CMAP responses confirm that there is no cross-activation between the proximal and distal cuffs, supporting the efficacy and specificity of our dual-stimulation paradigm. Figure 3c, Supplementary Fig. 13, and Supplementary Note 2 describe the setup and method for analyzing the electrical characteristics according to the stimulation group in the nerve injury model. Supplementary Note 2 describes the modeling method in detail.

The essential function is in the ability to deliver effective electrical stimulation to the nerve interface for promoting nerve regeneration. The RF power supplied to the transmission (T_x) coil is an important consideration. Figure 3d–f shows the voltage, current, and power (filled circle) delivered to the nerve for cases of PROX (blue) and DUAL (pink) stimulators as a function of input voltage (V_{in}) to the T_x coil, along with modeling results (dotted lines). Each input voltage corresponds to the input power, as shown in Supplementary Fig. 14. The data in Fig. 3d indicate that the V_{out} from the device at the nerve increases with V_{in} . The detailed measurement method is described in Note 2. Fig. 3e, f show agreement between experiment and simulation results for the current and power of the stimulation. Negligible differences exist between the magnitude of stimulation for the PROX and DUAL cases, thus verifying that the devices are suitable for comparing the results for these two cases.

For a given device and configuration of T_x and R_x coils, the magnitude of stimulation at the nerves depends on three parameters: the total resistance of the nerves R_{tot} , V_{in} and the wireless power transfer efficiency $\eta = |S_{21}|^2 \times 100\%$, obtained from the S-parameters in high-frequency electromagnetic finite element simulations (Supplementary Note 3 and Fig. 3g–i). Measurements indicate that R_{tot} are in the range of 3–6 k Ω at V_{in} of 3 V or higher (Fig. 3g). This result is within the commonly reported range for nerve impedance, on the order of several k Ω ^{23–26}. The left of Fig. 3h shows 3D electromagnetic finite element simulations of the wireless power transfer system, to capture the physics of inductive coupling between the T_x and R_x coils at 13.56 MHz, with the R_x coil vertically 3 mm above the T_x coil. The power transfer efficiency follows a nonlinear decay as the nerve resistance increases. Modeling results for relevant resistances indicate that the power transfer efficiency is between 0.75 and 1.5% (Fig. 3h, right), for a vertical separation distance of 3 mm, zero angular, and zero lateral misalignment between the coils.

The frequency-dependent response of the bioresorbable stimulator is modeled in the MHz range for variable resistances in the physiological range of interest 3–6 k Ω ; the S-parameters at resonance vary between –1.6 to –1.4 dB (Fig. 3i), and the power transfer efficiency varies between 0.75 to 1.5% (Fig. 3j). The details are in Note 3.

In vivo operation

Figure 4 summarizes the use of the device in a rodent model. The implantation procedure appears in Fig. 4a, b shows the circuit and block diagram. Activation occurs with the passage of RF current through the T_x coil (Supplementary Fig. 15a). Simulation results for the dual loop antenna (T_x coil) on the right side of Supplementary Fig. 15b show the magnetic field distribution. Supplementary Fig. 15c summarizes V_{out} at heights of 1, 3, and 5 cm from the T_x coil. The R_x coil is at a height of 3–5 cm when the rat is prone on the T_x coil. Supplementary Fig. 16 presents two methods for determining the optimal placement of the R_x coil. Activation of an LED connected to the R_x coil facilitates visual identification of the location of maximum η (Supplementary Fig. 16b). A voltmeter connected at the cuff electrode quantifies V_{out} (Supplementary Fig. 16c).

Evaluations of devices 1 (Fig. 4) and 2 (Supplementary Fig. 17) involve tests in two biologically independent rat models. Indicators of device lifetime and operational stability can be evaluated through changes in the input power to the T_x coil needed to achieve maximum CMAP amplitude (Fig. 4c and Supplementary Fig. 17a) and through changes in the CMAP amplitude for a fixed power of 2 W to the T_x coil (Fig. 4d). The T_x power necessary to achieve maximum CMAP amplitude gradually increases to 3 W over ~110 days for Device 1, and to 3.5 W over 107 days for Device 2 (Fig. 4c). For a fixed power of 2 W, Devices 1 and 2 maintain at least 80% of the maximum CMAP values for ~90 and 70 days, respectively (Fig. 4d and Supplementary Fig. 17b). In these cases, increasing the input power to 3.5–4 W enables stimulation at maximum CMAP amplitudes for 130 days for Device 1 and 110 days for Device 2. Beyond 136 days for Device 1 and 114 days for Device 2, the devices fail to induce measurable amplitudes even at a power of 10 W, mainly due to mechanical damage in the extension electrode area (Supplementary Fig. 10 and Supplementary Fig. 18) and dissolution of PLGA at the cuff and electrode connections.

The biocompatibility of the implanted device and the nerve tissue damage following electrical stimulation was evaluated 2 weeks after the device implantation by assessing fibrosis thickness around the cuff and the number of macrophages and apoptotic cells inside the nerve. The fibrotic collagen layer thickness was approximately 200 μm due to the foreign body reaction following cuff electrode implantation, and there was no significant difference in the encapsulation thickness depending on the presence or absence of electrical stimulation (Supplementary Fig. 19a, b). In addition, the number of macrophages and the number of apoptotic cells in the

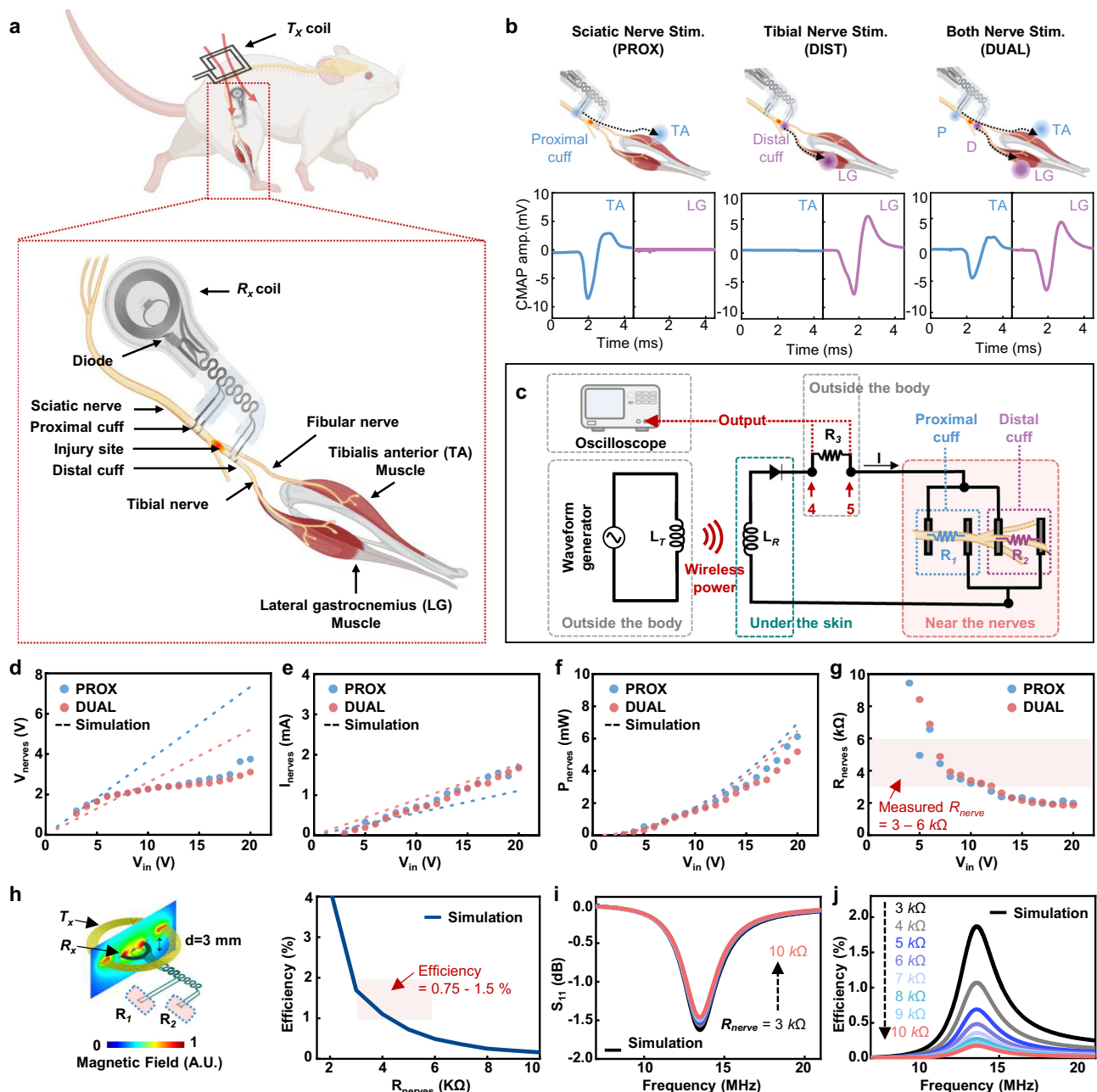


Fig. 3 | In vivo acute tests for characterization of wireless bioresorbable dual stimulators in a rodent model. **a** Schematic illustration of the implantation location. Top: Placement of the device in the animal and wireless coupling to an external transmission (T_x) coil. Bottom: Device with cuffs wrapped around the sciatic nerve (proximal cuff) and tibial nerve branch (distal cuff). Due to a trans-connection between the cuffs on the tibial nerve, the proximal cuff only stimulates the TA through the fibular nerve branch. The distal cuff uniquely stimulates the LG. R_x = receiver. T_x = transmission. [Created with Biorender.com]. **b** Schematic illustration of the experimental design (top) and EMG signals from the TA and LG muscles for each case. Corresponding changes in CMAP amplitude (bottom). TA: tibialis anterior, LG: lateral gastrocnemius, CMAP: compound muscle action potential, SHAM: no stimulation using a sham device model, PROX: stimulation of only the proximal

sciatic nerve, DUAL: stimulation of both the proximal sciatic nerve and the distal tibial nerve. [Created with Biorender.com]. **c** Circuit and block diagrams of the wireless stimulation system. A resistor (R_3) facilitates measurements of the change in voltage between points 4 and 5 as a function of input voltage. **d–g** Voltage (**d**), current (**e**), and power (**f**) applied to the nerve, and (**g**) resistance of the nerve as a function of input voltage after nerve damage, as determined through in vivo tests. **h** Schematic illustration and modeling results for the magnetic inductive coupling between a T_x coil and the R_x coils (left). Modeling results for the efficiency of power transfer as a function of the resistance of the nerve (R_{nerve}) (right). **i, j** Modeling results for the efficiency (**i**) and the reflection coefficient as a function of frequency (**j**) for various values of R_{nerve} .

nerve were analyzed through immunofluorescence staining (IF) and TUNEL staining targeting CD68 and fragmented DNA, respectively (Supplementary Fig. 19c–f). The expression of CD68, markers of total macrophages, was minimal in all groups and had no significant difference (Supplementary Fig. 19c, d). Fragmented DNA-stained cell death was observed to be less than 1% and had no significant

difference in all groups (Supplementary Fig. 19e, f). This indicates that cuff implantation maintains low cytotoxicity and high biocompatibility with surrounding tissues, and that electrical stimulation does not cause significant tissue damage.

At 4- and 32-weeks post-implantation, blood chemistry evaluations indicate that most parameters remain within normal ranges

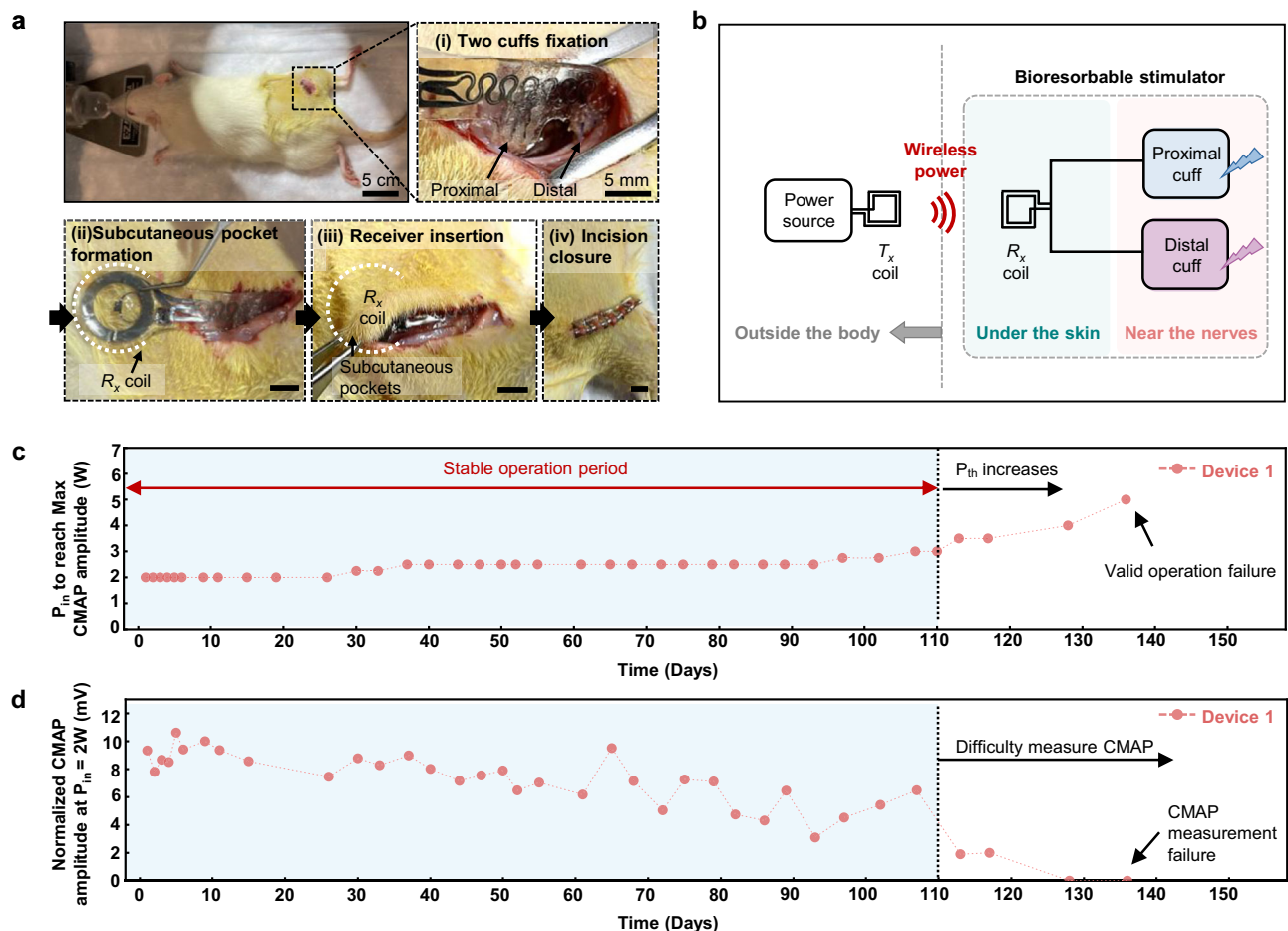


Fig. 4 | In vivo tests of a wireless bioresorbable dual-stimulator in a rodent model. **a** Surgical procedure for implantation. From left to right: an incision in the skin allows attachment of the stimulation cuffs to the sciatic nerve and tibial nerve branch; a subcutaneous pocket forms a point of insertion for the radio frequency (RF) harvester and its connection to the cuffs through serpentine traces; the R_x coil resides in the subcutaneous space; sutures and clips close the muscle

and the skin, respectively; passing RF current through the T_x coil activates stimulation. **b** Circuit and block diagram of the system. **c** Changes in minimum input power required to achieve maximum CMAP amplitude and **(d)** normalized changes in CMAP amplitude under the lowest RF power to the T_x coil (2 W), for $n=3$. R_x = receiver. T_x = transmission.

relative to controls, consistent with the biocompatibility of the implanted device (Supplementary Fig. 20). Key blood chemistry markers at 4 weeks—creatinine (CREA), total protein (TP), albumin (ALB), glucose (GLU), alanine aminotransferase (ALT), alkaline phosphatase (ALP), and total bilirubin (TBIL)—exhibit no significant differences from controls, suggesting no adverse organ toxicity and preserved renal, hepatic, and metabolic functions (Supplementary Fig. 20a). Supplementary Fig. 20b summarizes blood chemistry parameters including white blood cell (WBC), hemoglobin (HGB), mean corpuscular volume (MCV), and platelet (PLT) counts at 4- and 32-weeks post-implantation. Initially, WBC and PLT counts exhibit a slight difference 4 weeks after surgery, likely reflecting an early immune response, but subsequently stabilize or return to control levels by 32 weeks.

Early regeneration: dual stimulation to prevent muscle atrophy immediately following nerve injury

Examination of denervated muscles early after nerve injury provides information on muscle retention and the ability of the muscle to prevent atrophy²⁷. As illustrated in Fig. 5a, ultrasound images of LGs demonstrate that DUAL rats (0.91 ± 0.08 , $n=6$) have a significantly higher cross-sectional area (CSA) than PROX animals (0.79 ± 0.06 , $n=7$) [$p=0.0049$] one week after injury. DUAL also have a larger average CSA than SHAM (0.83 ± 0.05 ,

$n=8$) [$p=0.0334$] (Fig. 5b). At 1-week post-injury, DUAL rats maintain the largest muscle CSA. Histological analysis of MG fibers 2 weeks after injury shows that DUAL stimulation (707 ± 120 , $n=8$) leads to a significantly higher fiber CSA than both PROX stimulation (563 ± 167 , $n=9$) and SHAM (non-stimulated) (449 ± 125 , $n=10$) [$p=0.0449$ for PROX; $p=0.0007$ for SHAM] (Fig. 5c). These results indicate that dual stimulation maximizes the therapeutic outcome of electrical stimulation to prevent muscle atrophy immediately after nerve injury.

Late regeneration: improved muscle reinnervation 6 weeks post-injury

Electrophysiological and histological measurements of reinnervated muscle 6 weeks after injury highlight the effects of treatment. Based on ultrasound imaging, the CSA of the ipsilateral LG at 6 weeks after injury reveals no significant differences between treatment groups at this time point. The DUAL (0.77 ± 0.10 , $n=11$) rats show a larger average LG CSA than SHAM (0.72 ± 0.04 , $n=12$), although not statistically significant [$p=0.07$] (Fig. 6a). The average of PROX rats is 0.72 ± 0.05 ($n=11$). At the same time point, histological analysis of MG fibers show that both DUAL (1049 ± 195 , $n=11$) and PROX (1060 ± 252 , $n=11$) animals have significantly higher fiber CSA than SHAM animals (770 ± 148 , $n=12$) [$p=0.0040$ for DUAL, $p=0.0016$ for PROX] (Fig. 6b). The data indicate no difference in mean CSA between DUAL and PROX

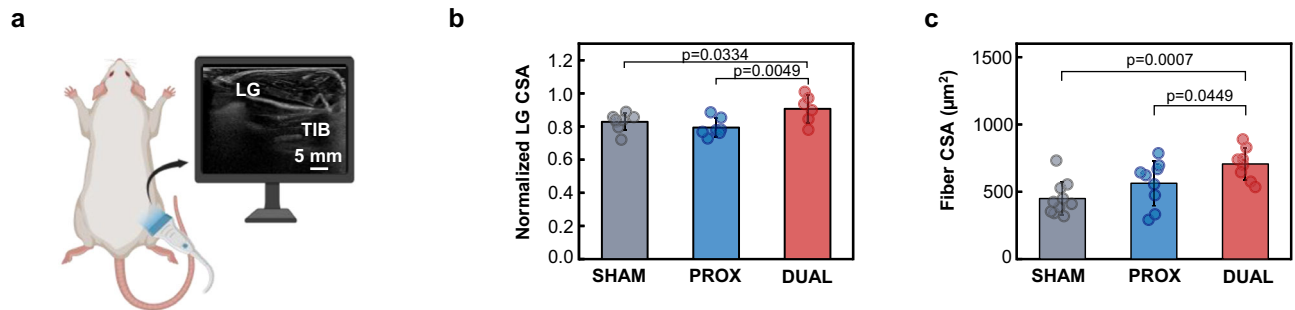


Fig. 5 | Effects of dual electrical stimulation on preventing muscle atrophy during the early stages of nerve injury. **a** Schematic of ultrasound acquisition and representative ultrasound image of the LG in cross-section. TIB Tibia. [Created with Biorender.com]. **b** Normalized ultrasound CSA of ipsilateral LG muscle to contralateral 1 week after injury. SHAM ($n=8$); PROX ($n=7$); DUAL ($n=6$). **c** Muscle fiber CSA of MG 2 weeks post-injury. SHAM

($n=10$); PROX ($n=9$); DUAL ($n=8$). n biologically independent animals. A one-way ANOVA with Fisher's LSD post hoc was used to determine the effect of treatment. Data were expressed as mean \pm SEM. CSA cross-sectional area, LG lateral gastrocnemius, MG medial gastrocnemius. SHAM no stimulation using a sham device model, PROX stimulation of only the proximal sciatic nerve, DUAL stimulation of both the proximal sciatic nerve and the distal tibial nerve.

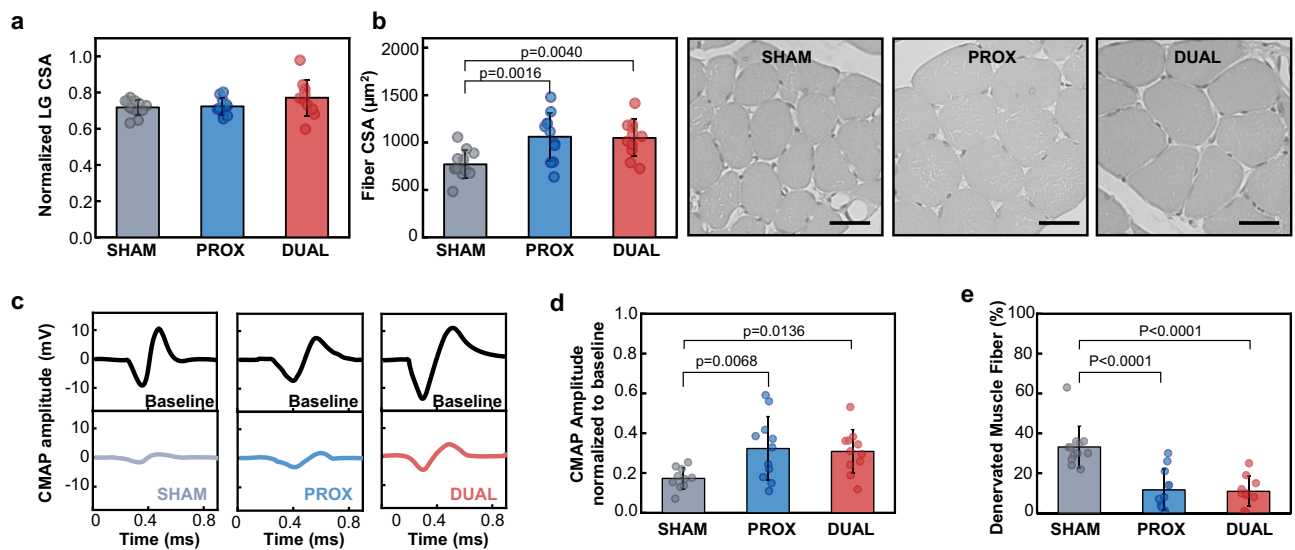


Fig. 6 | Effects of proximal and dual electrical stimulation on muscle reinnervation 6 weeks after injury. **a** Ultrasound CSA of ipsilateral LG normalized to the contralateral at 6 weeks. SHAM ($n=12$); PROX ($n=11$); DUAL ($n=11$). **b** Muscle fiber CSA of MG 6 weeks post-injury, plus example images of MG sections stained with Hematoxylin and Eosin (H&E) for each treatment. Scale bars, 30 μm . **c** Representative 6-week CMAP traces (bottom, colored waveform) are baseline traces (top, black waveform) for each treatment. Scale bar, 2 mV (vertical), 0.2 ms (horizontal). **d** CMAP amplitude of LG 6 weeks after injury,

normalized to baseline values. SHAM ($n=10$); PROX ($n=11$); DUAL ($n=11$). n biologically independent animals. **e** Percentage of small, angulated muscle fibers (less than 250 μm^2) in MG 6 weeks post-injury. SHAM ($n=12$); PROX ($n=11$); DUAL ($n=10$). n biologically independent animals. A one-way ANOVA with Fisher's LSD post hoc was used to determine the effect of treatment. Data were expressed as mean \pm SEM. CSA cross-sectional area. LG lateral gastrocnemius, MG medial gastrocnemius, CMAP compound muscle action potential. SHAM no stimulation using a sham device model. PROX stimulation of only the proximal sciatic nerve. DUAL stimulation of both the proximal sciatic nerve and the distal tibial nerve.

[$p=0.89$]. Figure 6c shows 6-week CMAP responses to direct electromyographic (EMG) stimulation of the sciatic nerve for assessing muscle reinnervation. At six weeks after injury, both DUAL (0.31 ± 0.11 , $n=11$) and PROX (0.32 ± 0.16 , $n=11$) animals show greater recovery than SHAM (0.17 ± 0.058 , $n=10$) [$p=0.0136$ for DUAL and 0.0068 for PROX]. DUAL and PROX have similar averages and are not significantly different [$p=0.77$] (Fig. 6d).

Further examination, six weeks after injury, focuses on the percentage of MG muscle fibers that were denervated, out of a total of more than 200 fibers per animal. These fibers are angular and measure less than 250 μm^2 in size, as shown in Supplementary Fig. 21. SHAM (33 ± 10 , $n=12$) animals show significantly higher percentage of denervated fibers than both DUAL (11 ± 7.5 , $n=10$) and PROX (11.6 ± 10 , $n=11$) [$p<0.0001$ for DUAL, $p<0.0001$ for PROX]. DUAL and PROX show no significant differences in their averages [$p=0.86$] (Fig. 6e).

In summary, dual electrical stimulation is effective in preventing muscle atrophy in rodents immediately after nerve injury and effectively enhances muscle reinnervation in the later stage of recovery, 6 weeks after injury.

Discussion

This study demonstrates that the bioresorbable wireless stimulators can be engineered to allow simultaneous operation at multiple sites, with stable outputs for up to several months. In dual-stimulator designs applied to peripheral nerves, animal model studies indicate capabilities in the prevention of early muscle atrophy following a PNI and to accelerate muscle reinnervation. These advances have broad implications in resorbable implants as bioelectronic medicines, configured to operate over a timeframe aligned with a clinical need and then to disappear, as a mechanism to avoid the requirement for surgical extraction

procedures. Other clinical applications requiring long-term treatments with bioresorbable devices, including long-term nerve regeneration, appear to be promising targets for future research.

Methods

Preparing the bioresorbable wireless dual stimulator

Fabricating and encapsulating the electronics. To prepare polyurethane (PU) 75, 2.7 g of polycaprolactone triol (PCL-triol, average Mn ~900 g/mol; DAICEL) melted at -60 °C. After complete melting, 540 μ L of hexamethylene diisocyanate (HDI; Sigma-Aldrich) was added, and the mixture was further heated at 60 °C for 15 min. Anhydrous butyl acetate (15 mL; Sigma-Aldrich) was then added, and the solution was mixed thoroughly using a vortex. Tin(II) 2-ethylhexanoate (Sn(Oct)₂, 6.53 μ L; Sigma-Aldrich) was introduced as a catalyst. The resulting solution was drop-cast onto a silicon (Si) wafer and dried overnight at -60 °C to form a PU film. A mixture of 1,3,5-triallyl-1,3,5-triazine-2,4,6-(1H,3H,5H)-trione (TTT; Sigma-Aldrich), 4-pentenoic acid (4PA; Sigma-Aldrich), and 1,4-butanediol diacrylate (BDT; Sigma-Aldrich) at a molar ratio of 1:4:7 formed the polyanhydride (PA) precursor solution. Based on 0.46 g of 4PA, the formulation included 27 mg of 2,2-dimethoxy-2-phenylacetophenone (DMPA; Sigma-Aldrich) as a photoinitiator. Drop-casting a 5 wt% solution of poly(lactic-co-glycolic acid) (PLGA; 75:25, (lactide:glycolide); Sigma-Aldrich) in ethyl acetate onto a Si wafer produced a uniform film, which dried overnight in a fume hood. A biodegradable W/wax conductive paste composed of tungsten (W) microparticles (2–4 μ m; Buffalo Tungsten) and candelilla wax at a weight ratio of -10:1 formed²⁸.

Details on the process appear in Supplementary Fig. 2. The Mo structure consisted of two layers, referred to as the bottom and top in the following. Laser-cut Mo foils (15- μ m thick; Goodfellow) formed R_x coils along with structures for the extension and cuff electrodes. The PU and PA substrates offered sufficient adhesion to the Mo foil to prevent its movement during the laser-cutting process. The top electrode design aligns with the bottom using three alignment markers, producing a dual stimulator with stacked extension electrodes of the same width as those in a single stimulator.

Forming vias for the R_x coils. The regions of the R_x coils include a central interlocking fold structure. This design mechanically connects the top and bottom coil layers, forming a robust interlocking bond when folded. Biodegradable W/wax paste completes the electrical connections, finalizing the R_x coil. The detailed procedures in folding and bonding appear in Supplementary Fig. 4.

Fabricating and integrating the diode. Preparation of transient PIN (p-type–intrinsic–n-type) diode involved solid-state diffusion of phosphorus (950 °C in a tube furnace with N_2 flow) and boron (1000 °C in a tube furnace with N_2 flow) onto silicon-on-insulator (SOI) wafers (top silicon 5.0- μ m thick, p-type, 1–10 Ω -cm; Ultrasil LLC, US), with doping regions defined by photolithography and -320-nm-thick SiO₂ masks formed by plasma-enhanced chemical vapor deposition (PECVD); sequential patterning, BOE etching, and doping formed n^+ and p^+ regions, followed by removal of the buried oxide by hydrofluoric acid (HF) and deposition of insulating and contact metal layers^{8,11}. Information on the procedures for forming the diode connections are in Supplementary Fig. 8. Supplementary Fig. 8a–f summarizes the process for transferring the diodes to films of PA. Supplementary Fig. 8g–l highlights the diode connection pad, the method for mounting the diode into the pocket. Long-term performance and structural stability evaluations, including testing via structures, diode connection pads, mechanical durability, and defect detection, are discussed in detail in Supplementary Note 1.

Electromagnetic simulation

The electromagnetic performance of the T_x coil and the wireless power transfer system was modeled using the commercial software package ANSYS HFSS. This modeling determined the magnetic field and V_{out} to ensure sufficient energy transfer over the working range of the device. The dimensions of the two-loop T_x coil measured 15 cm \times 20 cm, and copper wire (AWG 12) used as the conductive element. A lumped port delivered 2 W of input power to the antenna, with input impedance matched at 13.56 MHz. Detailed simulation results and configuration are in the Supplementary Note 4.

In vivo studies using rat models

Device implantation. All animal use procedures were approved by Northwestern University's Institutional Animal Care and Use Committee (protocol IS00014691) and were performed in full compliance with the National Institutes of Health Guide for the Care and Use of Laboratory Animals and the guidelines of the National Society for Medical Research. The devices, sterilized with UV for 30 min prior to implantation, were surgically implanted into the right sciatic nerve of male and female Sprague-Dawley rats (250–300 g, Charles River Laboratories). The proximal cuff was wrapped around the sciatic nerve and the distal cuff was secured to the tibial nerve branch (see Figs. 3a, 4a and Supplementary Note 5).

Wireless operation. Power was delivered wirelessly to the device using a commercial RF system (NeuroLux, Inc., Evanston, IL). Experimental animals were divided into three electrical stimulation groups (Fig. 3b): (1) no stimulation using a sham device model (SHAM), (2) stimulation of only the proximal sciatic nerve (PROX), and (3) stimulation of both the proximal sciatic nerve and the distal tibial nerve (DUAL). Therapeutic electrical stimulation was performed for 1 h per day for 6 days with a pulse width of 200 μ s, a frequency of 20 Hz, and a minimum amplitude above threshold of 2–4 V (See Supplementary Table 6 for stimulation parameters). A 6-day therapeutic electrical stimulation protocol was selected as it has been identified as optimal for rat sciatic nerve injury recovery in previous studies^{6,29}. Additionally, while a range of parameters have been effective in promoting axon regeneration (3–100 Hz frequency, 100–400 μ s pulse width, and 0.2–3 V)³⁰, the selected protocol is the same as previously used by our group⁶.

Evaluation. Two groups of animals were evaluated at endpoints of 2 and 6 weeks ($n = 27$ and $n = 34$, respectively). Six weeks was chosen as an intermediate recovery time point to assess therapeutic effects before full recovery occurs, avoiding ceiling effects while accounting for the prolonged regeneration timeline in rat models of nerve transection and repair^{31–33}. Each stimulation group maintained a similar ratio of male and female rats (Supplementary Table 7).

Histological analysis

Processing of the tissue. Animals were sacrificed and intracardially perfused with phosphate-buffered saline, followed by 4% paraformaldehyde. MGs were then immersed in 4% paraformaldehyde for 24 h, 30% sucrose solution for 24 h, and were snap-frozen in Tissue Freezing Material (TFM-C, Thermo Fisher Scientific) immersed in isopentane cooled by liquid nitrogen. MGs were sectioned into 16- μ m-thick transverse sections on a cryostat (CM3050S, Leica).

Ultrasound imaging of cross-sectional areas. Ultrasound images were captured using a Logiq Ultrasound System (P9 XDclear, General Electric) with a Matrix Linear Array Probe (ML6-15L, General Electric) (Fig. 5a). Animals were anesthetized and three images were taken of each LG and averaged to attain the cross-sectional area (CSA) at each time point. The ipsilateral CSA was normalized to the contralateral to account for sex differences in animal size. For the early regeneration study

results (Fig. 5b), normalized 1-week values were compared between male and female rats using a two-way ANOVA. No effect of sex was found, so the data were combined for each treatment [$p = 0.284$]. In the late regeneration study results (Fig. 6a), a two-way ANOVA also revealed no significant effect of sex, so data were combined [$p = 0.119$].

Analyzing muscle fiber. To determine the fiber CSA, MGs were stained with CollIV (ab6586, Abcam) and imaged at 20x (DM6000 B, Leica). For each animal, four random sections of the muscle were captured, and 400 muscle fiber areas were averaged using ImageJ. In the early regeneration study results (Fig. 5c), fiber CSA values were compared between males and females using a two-way ANOVA, and no significant effect of sex was found, so data were combined for each treatment [$p = 0.8425$]. In the late regeneration study results (Fig. 6b), a two-way ANOVA showed a significant effect of sex, but data were combined due to an equivalent ratio of both sexes for all treatments [$p = 0.03743$].

Additionally, small angulated fibers (less than $250 \mu\text{m}^2$) consistent with chronic denervation were also quantified. Four sections were randomly captured, and each was blindly evaluated for the percentage of denervated muscle fibers by a board-certified neuromuscular medicine physician trained in neuromuscular pathology, and the values were averaged. A two-way ANOVA confirms that there is no effect of sex, so the data from males and females are combined for each treatment [$p = 0.45$].

Electrophysiology measurements

After anesthetizing the animals, CMAP amplitudes were measured using EMG with a 1-inch, 30-gauge concentric needle electrode connected to a clinical-grade Nicolet EDX system with Synergy software (Natus Neurology, Middleton, WI). In Supplementary Fig. 26, data showed a robust correlation between electrophysiological and behavioral outcomes, making CMAP an effective indicator of functional muscle recovery in our experimental paradigm (experimental setup described in Supplementary Note 7 as well as aligning with current clinical practice in assessment of nerve injuries³⁴). Measurements of LG maximum amplitude were taken prior to nerve injury to account for variability in pre-injury maximum CMAP amplitude among rats, setting this as the baseline. The maximum CMAP amplitude values measured 6 weeks after device implantation and nerve injury were normalized to the pre-injury baseline. Thus, the observed recovery was relative to each animal's baseline, considering the maximum innervation potential of the individual rat.

To account for sex differences, 6-week values were normalized to baseline. These values were evaluated for sex differences using a two-way ANOVA, but none were found [$p = 0.165$]. Therefore, sexes were combined for each treatment.

Statistical analysis

A priori power analysis (performed in G-Power) determined the number of animals needed ($n = 44$) to adequately power a one-way ANOVA comparison with an effect size of 0.5, and $\alpha = 0.05$. For statistical analyses, the α level was set to 0.05. Results are expressed as mean values with one standard deviation. Two-way ANOVAs were utilized to assess sex differences for each outcome, and males and females were combined for each treatment. Then, one-way ANOVAs were used to determine the effects of treatment, followed by a Fisher LSD post hoc test. All treatment groups (SHAM, PROX, and DUAL) were included in the data analysis.

Ethics declarations

Every experiment involving animals have been carried out following a protocol approved by an ethical commission (protocol IS00014691).

Reporting summary

Further information on research design is available in the Nature Portfolio Reporting Summary linked to this article.

Data availability

The data that support the findings of this study are available within the main text and the Supplementary Information. The data generated for the studies shown in Figs. 1–6 are provided in the Supplementary Information/Source data files. All data are also available from the corresponding authors upon request. Source data are provided with this paper.

References

- Hardy, P. B., Wang, B. Y., Chan, K. M., Webber, C. A. & Senger, J. L. B. The use of electrical stimulation to enhance recovery following peripheral nerve injury. *Muscle Nerve* **70**, 1151–1162 (2024).
- Gordon, T., Amirjani, N., Edwards, D. C. & Chan, K. M. Brief post-surgical electrical stimulation accelerates axon regeneration and muscle reinnervation without affecting the functional measures in carpal tunnel syndrome patients. *Exp. Neurol.* **223**, 192–202 (2010).
- Wong, J. N., Olson, J. L., Morhart, M. J. & Chan, K. M. Electrical stimulation enhances sensory recovery: a randomized controlled trial. *Ann. Neurol.* **77**, 996–1006 (2015).
- Power, H. A., Morhart, M. J., Olson, J. L. & Chan, K. M. Postsurgical electrical stimulation enhances recovery following surgery for severe cubital tunnel syndrome: a double-blind randomized controlled trial. *Neurosurgery* **86**, 769–777 (2020).
- Barber, B. et al. Intraoperative brief electrical stimulation of the spinal accessory nerve (BEST SPIN) for prevention of shoulder dysfunction after oncologic neck dissection: a double-blinded, randomized controlled trial. *J. Otolaryngol. Head. Neck Surg.* **47**, 7 (2018).
- Koo, J. et al. Wireless bioresorbable electronic system enables sustained nonpharmacological neuroregenerative therapy. *Nat. Med.* **24**, 1830–1836 (2018).
- Guo, H. et al. Advanced materials in wireless, implantable electrical stimulators that offer rapid rates of bioresorption for peripheral axon regeneration. *Adv. Funct. Mater.* **31**, 2102724 (2021).
- Choi, Y. S. et al. Stretchable, dynamic covalent polymers for soft, long-lived bioresorbable electronic stimulators designed to facilitate neuromuscular regeneration. *Nat. Commun.* **11**, 5990 (2020).
- Kang, S.-K. et al. Bioresorbable silicon electronic sensors for the brain. *Nature* **530**, 71–76 (2016).
- Lee, G. et al. A bioresorbable peripheral nerve stimulator for electronic pain block. *Sci. Adv.* **8**, eabp9169 (2022).
- Hwang, S.-W. et al. A physically transient form of silicon electronics. *Science* **337**, 1640–1644 (2012).
- Hafeman, A. E. et al. Injectable biodegradable polyurethane scaffolds with release of platelet-derived growth factor for tissue repair and regeneration. *Pharm. Res.* **25**, 2387–2399 (2008).
- Song, J. W. et al. Bioresorbable, wireless, and battery-free system for electrotherapy and impedance sensing at wound sites. *Sci. Adv.* **9**, eade4687 (2023).
- Huang, Y. et al. Bioresorbable thin-film silicon diodes for the optoelectronic excitation and inhibition of neural activities. *Nat. Biomed. Eng.* **7**, 486–498 (2023).
- Jain, J. P. et al. Role of polyanhydrides as localized drug carriers. *J. Control. Release* **103**, 541–563 (2005).
- Edlund, U. et al. Sterilization, storage stability and in vivo biocompatibility of poly (trimethylene carbonate)/poly (adipic anhydride) blends. *Biomaterials* **21**, 945–955 (2000).
- Saleh, B. E. A. & Teich, M. C. *Fundamentals of photonics* (John Wiley & Sons, 2019).
- Rabus, D. G. et al. High-Q channel-dropping filters using ring resonators with integrated SOAs. *IEEE Photon. Technol. Lett.* **14**, 1442–1444 (2002).
- Choi, Y. S. et al. Biodegradable polyanhydrides as encapsulation layers for transient electronics. *Adv. Funct. Mater.* **30**, 2000941 (2020).

20. Lee, S. et al. Metal microparticle–polymer composites as printable, bio/ecoresorbable conductive inks. *Mater. Today* **21**, 207–215 (2018).
21. Spr Therapeutics. Sprint PNS system. <https://www.sprtherapeutics.com> (2025).
22. Synapse Biomedical. TransAeris System. <https://www.synapsebiomedical.com> (2025).
23. Sakuma, M. et al. Chronic electrical nerve stimulation as a therapeutic intervention for peripheral nerve repair. *Bioelectron. Med.* **2**, 43–48 (2015).
24. Lee, S. et al. Development of battery-free neural interface and modulated control of tibialis anterior muscle via common peroneal nerve based on triboelectric nanogenerators (TENGs). *Nano Energy* **33**, 1–11 (2017).
25. Wu, P. et al. Ultrasound-driven in vivo electrical stimulation based on biodegradable piezoelectric nanogenerators for enhancing and monitoring the nerve tissue repair. *Nano Energy* **102**, 107707 (2022).
26. Lienemann, S. et al. Stretchable gold nanowire-based cuff electrodes for low-voltage peripheral nerve stimulation. *J. Neural Eng.* **18**, 045007 (2021).
27. Chan, K., Curran, M. & Gordon, T. The use of brief post-surgical low frequency electrical stimulation to enhance nerve regeneration in clinical practice. *J. Physiol.* **594**, 3553–3559 (2016).
28. Won, S. M. et al. Natural wax for transient electronics. *Adv. Funct. Mater.* **28**, 1801819 (2018).
29. Birenbaum, N. K. et al. Multiple sessions of therapeutic electrical stimulation using implantable thin-film wireless nerve stimulators improve functional recovery after sciatic nerve isograft repair. *Muscle Nerve* **67**, 244–251 (2023).
30. Bordett, R. et al. Advancements in stimulation therapies for peripheral nerve regeneration. *Biomed. Mater.* **19**, 052008 (2024).
31. Kemp, S. W. P. et al. Functional recovery following peripheral nerve injury in the transgenic Thy1-GFP rat. *Peripher. Nerv. Syst.* **18**, 220–231 (2013).
32. Asensio-Pinilla, E. et al. Electrical stimulation combined with exercise increase axonal regeneration after peripheral nerve injury. *Exp. Neurol.* **219**, 258–265 (2009).
33. Nadeau, J. R. et al. Acute intermittent hypoxia enhances regeneration of surgically repaired peripheral nerves in a manner akin to electrical stimulation. *Exp. Neurol.* **341**, 113671 (2021).
34. Pripotnev, S. et al. Interpreting electrodiagnostic studies for the management of nerve injury. *J. Hand Surg.* **47**, 881–889 (2022).
35. Shin, J. et al. Bioresorbable pressure sensors protected with thermally grown silicon dioxide for the monitoring of chronic diseases and healing processes. *Nat. Biomed. Eng.* **3**, 37–46 (2019).

Acknowledgements

This work was supported by the Querrey-Simpson Institute for Bioelectronics at Northwestern University. J.A.R. and S.L. acknowledge support from National Institutes of Health grants (R01NS126918). C.K.F. acknowledges support from the National Institute of Neurological Disorders and Stroke (R01NS136683), Eunice Kennedy Shriver National Institute of Child Health and Human Development (R03HD101090), the American Neuromuscular Foundation (Development Grant), and the Belle Carnell Regenerative Neurorehabilitation Fund at the Shirley Ryan AbilityLab. H.-Y. A. acknowledges support by a grant of the Korea Health Technology R&D Project through the Korea Health Industry Development Institute (KHIDI), funded by the Ministry of Health & Welfare, Republic of Korea (HI19C1348). R.A. acknowledges support

from the ASME Applied Mechanics Division - Haythornthwaite Foundation Research Initiation Grant. We thank K.E. Madsen for helpful discussions regarding electrochemistry. Small animal imaging work was supported by the Center for Translational Imaging at Northwestern University. Figs. 3a, b, 5a and Supplementary Figs. 10c, 15b created with BioRender.com released under a Creative Commons Attribution-NonCommercial-NoDerivs 4.0 International license (<https://creativecommons.org/licenses/by-nc-nd/4.0/deed.en>)

Author contributions

H.-Y.A., J.B.W., C.F.K., and J.A.R. conceived the concept and designed the overall research; H.-Y.A. designed, developed, and characterized the long-term stable operating device and process; H.-Y.A., J.B.W., S.O., S.S., J.K., J.P., S.Y., Y.C., T.K., J.L., J.-Y.Y., O.R.W., D.D., C.P., G.L., D.C., W.-Y.M., H.Y., G.W., Y.B., J.T., T.C.C., S.W.J., S.L., C.F.K., and J.A.R. investigated and performed the experiments; H.-Y. A. and J.B.W. conducted the data analysis; R.A. and Y. H. performed the modeling and simulations; H.-Y. A., J.B.W., C.F.K., and J.A.R. wrote the manuscript.

Competing interests

The authors declare no competing interests.

Additional information

Supplementary information The online version contains supplementary material available at <https://doi.org/10.1038/s41467-025-59835-7>.

Correspondence and requests for materials should be addressed to Colin K. Franz or John A. Rogers.

Peer review information *Nature Communications* thanks Shirong Wang and the other, anonymous, reviewers for their contribution to the peer review of this work. A peer review file is available.

Reprints and permissions information is available at <http://www.nature.com/reprints>

Publisher's note Springer Nature remains neutral with regard to jurisdictional claims in published maps and institutional affiliations.

Open Access This article is licensed under a Creative Commons Attribution-NonCommercial-NoDerivatives 4.0 International License, which permits any non-commercial use, sharing, distribution and reproduction in any medium or format, as long as you give appropriate credit to the original author(s) and the source, provide a link to the Creative Commons licence, and indicate if you modified the licensed material. You do not have permission under this licence to share adapted material derived from this article or parts of it. The images or other third party material in this article are included in the article's Creative Commons licence, unless indicated otherwise in a credit line to the material. If material is not included in the article's Creative Commons licence and your intended use is not permitted by statutory regulation or exceeds the permitted use, you will need to obtain permission directly from the copyright holder. To view a copy of this licence, visit <http://creativecommons.org/licenses/by-nc-nd/4.0/>.

© The Author(s) 2025

¹Querrey Simpson Institute for Bioelectronics, Northwestern University, Evanston, IL 60208, USA. ²Center for Bio-Integrated Electronics, Northwestern University, Evanston, IL 60208, USA. ³Regenerative Neurorehabilitation Laboratory, Shirley Ryan AbilityLab, Chicago, IL, USA. ⁴Department of Mechanical Engineering, Rice University, Houston, TX 77005, USA. ⁵Division of Electrical Engineering, Hanyang University ERICA, Ansan 15588, Republic of Korea. ⁶College of Biomedical Science and Health, Inje University, Gimhae 50834, Republic of Korea. ⁷Department of Materials Science and Engineering, Yonsei

University, Seoul 03722, Republic of Korea. ⁸Department of Semiconductor Convergence Engineering, Sungkyunkwan University, Suwon 16417, Republic of Korea. ⁹Department of Chemical Engineering, Kyungpook National University, Daegu 41566, Republic of Korea. ¹⁰Thin Film Materials Research Center, Korea Research Institute of Chemical Technology, Daejeon 34114, Republic of Korea. ¹¹Advanced Materials and Chemical Engineering, University of Science and Technology, Daejeon 34113, Republic of Korea. ¹²Department of Electronic Engineering, Gachon University, Seongnam 13120, Republic of Korea. ¹³Department of Semiconductor Engineering, Gachon University, Seongnam 13120, Republic of Korea. ¹⁴Department of Bioengineering, Samueli School of Engineering, University of California Los Angeles, Los Angeles, CA 90095, USA. ¹⁵Division of Microsurgery, Department of Orthopedics, E-Da Hospital, I-Shou University Kaohsiung, Kaohsiung 824005, Taiwan. ¹⁶Division of Plastic Surgery, Feinberg School of Medicine, Northwestern University, Chicago, IL 60611, USA. ¹⁷Biologics Laboratory, Shirley Ryan AbilityLab, Chicago, IL 60611, USA. ¹⁸Department of Medicine, David Geffen School of Medicine, University of California Los Angeles, Los Angeles, CA 90095, USA. ¹⁹Eli and Edythe Broad Center of Regenerative Medicine and Stem Cell Research, University of California, Los Angeles, Los Angeles, CA 90095, USA. ²⁰Jonsson Comprehensive Cancer Center, David Geffen School of Medicine, University of California, Los Angeles, Los Angeles, CA 90095, USA. ²¹Department of Mechanical Engineering, Northwestern University, Evanston, IL 60208, USA. ²²Department of Materials Science and Engineering, Northwestern University, Evanston, IL 60208, USA. ²³Department of Civil and Environmental Engineering, Northwestern University, Evanston, IL 60208, USA. ²⁴Department of Physical Medicine and Rehabilitation, Northwestern University Feinberg School of Medicine, Chicago, IL 60611, USA. ²⁵Ken and Ruth Davee Department of Neurology, Northwestern University Feinberg School of Medicine, Chicago, IL 60611, USA. ²⁶Department of Biomedical Engineering, Northwestern University, Evanston, IL 60208, USA. ²⁷Department of Neurological Surgery, Feinberg School of Medicine, Northwestern University, Chicago, IL 60611, USA. ²⁸These authors contributed equally: Hak-Young Ahn, Jordan B. Walters. ✉e-mail: cf Franz@sralab.org; jrogers@northwestern.edu